Nanoscale Conductivity Imaging of Correlated Electronic States in WSe_2/WS_2 Moiré Superlattices

Zhaodong Chu,[1,*] Emma C. Regan,[2,3,4,*] Xuejian Ma,[1] Danqing Wang,[2,3,4] Zifan Xu,[1] M. Iqbal Bakti Utama,[2,4,5] Kentaro Yumigeta,[6] Mark Blei,[6] Kenji Watanabe,[7] Takashi Taniguchi,[8] Sefaattin Tongay,[6] Feng Wang,[2,4,9,†] and Keji Lai[1,‡]

[1]*Department of Physics, The University of Texas at Austin, Austin, Texas 78712, USA*
[2]*Department of Physics, University of California at Berkeley, Berkeley, California 94720, USA*
[3]*Graduate Group in Applied Science and Technology, University of California at Berkeley, Berkeley, California 94720, USA*
[4]*Material Science Division, Lawrence Berkeley National Laboratory, Berkeley, California 94720, USA*
[5]*Department of Materials Science and Engineering, University of California at Berkeley, Berkeley, California 94720, USA*
[6]*School for Engineering of Matter, Transport and Energy, Arizona State University, Tempe, Arizona 85287, USA*
[7]*Research Center for Functional Materials, National Institute for Materials Science, 1-1 Namiki, Tsukuba 305-0044, Japan*
[8]*International Center for Materials Nanoarchitectonics, National Institute for Materials Science, 1-1 Namiki, Tsukuba 305-0044, Japan*
[9]*Kavli Energy NanoSciences Institute at University of California Berkeley and Lawrence Berkeley National Laboratory, Berkeley, California 94720, USA*

(Received 1 July 2020; accepted 2 October 2020; published 30 October 2020)

We report the nanoscale conductivity imaging of correlated electronic states in angle-aligned WSe_2/WS_2 heterostructures using microwave impedance microscopy. The noncontact microwave probe allows us to observe the Mott insulating state with one hole per moiré unit cell that persists for temperatures up to 150 K, consistent with other characterization techniques. In addition, we identify for the first time a Mott insulating state at one electron per moiré unit cell. Appreciable inhomogeneity of the correlated states is directly visualized in the heterobilayer region, indicative of local disorders in the moiré superlattice potential or electrostatic doping. Our work provides important insights on 2D moiré systems down to the microscopic level.

DOI: 10.1103/PhysRevLett.125.186803

The vertical stacking of two-dimensional (2D) materials with similar lattice constants at small twist angles produces long-wavelength moiré superlattices, which can substantially modify the electronic structures of individual layers [1–3]. As exemplified by the groundbreaking experiments [4–6] and subsequent works [7–12], a plethora of exotic behaviors such as Mott insulating states [4–9], superconductivity [5,7–9], magnetic phases [10–12], and quantum anomalous Hall effect [12] have been reported on twisted bilayer graphene near the magic angle and trilayer graphene–boron nitride moiré superlattices. Moiré systems composed of transition metal-dichalcogenide (TMD) heterostructures offer a complementary and equally important material platform to investigate the rich many-body phenomena [13]. Because of the strong spin-orbit coupling, only twofold degeneracy remains in the TMD-based moiré systems, giving rise to an ideal playground to simulate the Mott-Hubbard physics in 2D triangular lattices [13–18]. To date, evidence of charge ordering and correlated states at partial moiré band fillings has been reported in both homobilayer [16] and heterobilayer TMD superlattices [17,18], with many other novel electronic states expected to emerge [19].

Despite the rapid progress in the research of TMD-based correlated states, a critically missing element here is the real-space visualization of a highly resistive electronic phase in the moiré heterostructure and the study of its spatial homogeneity. It should be noted that the small twist-angle disorder, which has been recently mapped out in graphene moiré systems [20], may not be crucial in TMD heterostructures [16,21] due to the relatively large effective mass [22,23]. Spatially resolved investigations, on the other hand, may reveal local fluctuations of moiré potential or electrostatic doping in the 2D sheet. Moreover, a notable experimental challenge in the investigation of TMD moiré superlattices lies in the large metal-semiconductor contact resistances, especially at the low-density regime where correlation effects manifest themselves. As a result, optical measurements such as reflectance [17] and optically detected resistance and capacitance (ODRC) [18] are preferred over traditional transport techniques. However, these studies [16–18] only demonstrated the existence of correlated insulating states on the hole-doped side, leaving the correlation physics on conduction bands unexplored. A noncontact method that directly measures the electrical conductivity on both electron- and hole-doped sides is

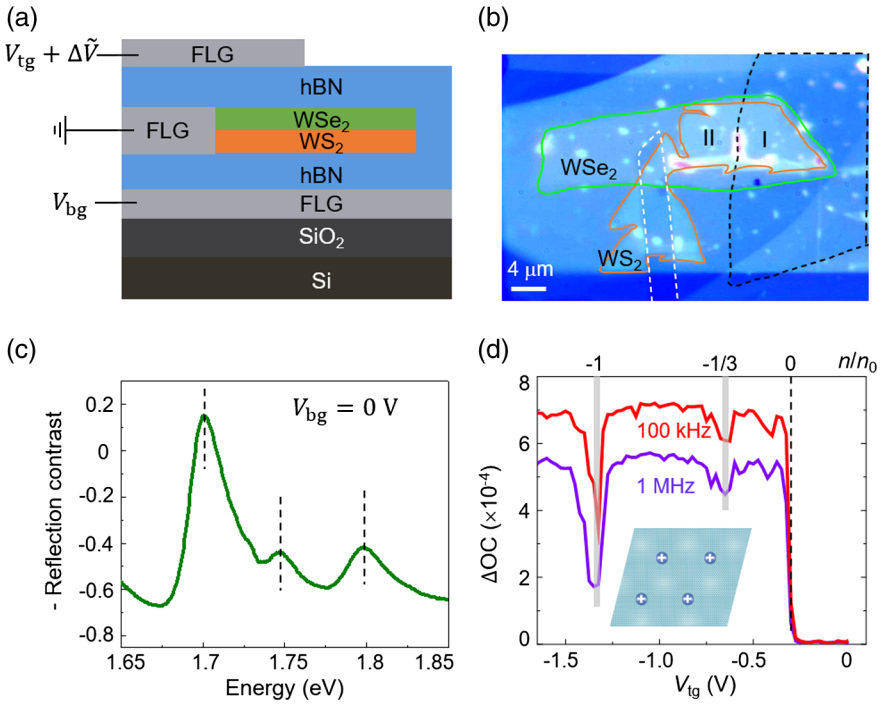

FIG. 1. (a) Schematic of the gated WSe_2/WS_2 superlattice device structure. The thicknesses of top and bottom HBN are 11 and 16 nm, respectively. (b) Optical microscopy image of the heterostructure device. The WSe_2, WS_2 monolayer flakes, FLG contact, and top gate are outlined in green, orange, white, and black, respectively. (c) Optical absorption spectrum in region II of the heterostructure in (b). The three peaks indicated by dashed lines are due to splitting of the WSe_2 A exciton, which is indicative of intralayer moiré excitons in the WSe_2/WS_2 superlattice. (d) ODRC signals at two different ac excitation frequencies as a function of the top-gate voltage and filling factors. The dashed line denotes the charge-neutral point (~ -0.3 V) and the shaded areas correspond to the Mott insulator state at $n/n_0 = -1$ and correlated insulating state at $-1/3$. The inset illustrates the Mott insulator state with one hole per moiré unit cell.

therefore desirable to understand the insulating nature of Mott-like states in these materials. In this Letter, we report the optical study and nanoscale conductivity imaging of angle-aligned WSe_2/WS_2 moiré heterobilayers by combining ODRC and microwave impedance microscopy (MIM) on the same devices. At sufficiently low temperatures, while the overall gate dependence of local conductivity in the monolayer regions are described by the ambipolar field effect, pronounced resistivity peaks on both electron and hole sides are observed in the superlattice area at certain moiré band fillings. The resistivity peak at one hole per lattice site is consistent with the Mott insulator state reported previously [17,18]. A resistivity peak at one electron per lattice site, on the other hand, is reported for the first time, which indicates that the Mott state is also present in electron-doped WS_2/WSe_2 moiré systems. In addition, the microwave images show clear spatial inhomogeneity of the correlated states, presumably due to local disorders in the moiré potential or electrostatic doping. Our results provide important insights for improving the quality of TMD moiré superlattices toward new discoveries in these fascinating material systems.

The samples in our study are WSe_2/WS_2 heterobilayers, which are encapsulated by top and bottom hexagonal boron nitride (HBN) dielectrics, as illustrated in Fig. 1(a). Few-layer graphene (FLG) layers are used as the gate and contact electrodes (see Supplemental Material for fabrication details [24]). The twist angle between the two monolayers is $\theta \sim 60°$ (see Fig. S2 in Ref. [24]), resulting in a moiré superlattice constant $L_M = a/\sqrt{\delta^2 + (\pi/3 - \theta)^2} \sim 8$ nm, where $\delta \sim 4\%$ is the lattice mismatch between monolayer WSe_2 ($a = 0.328$ nm) and WS_2 flakes. As seen in the optical image in Fig. 1(b), half of the heterostructure (region I) is covered by the top graphene layer, whereas the other half (region II) is not. Significant inhomogeneity due to trapped bubbles is observed in this heterostructure device. The optical absorption spectrum on region II [Fig. 1(c)] shows that the WSe_2 A exciton is split into three peaks, indicative of the presence of the moiré potential [31] (see more data in Fig. S3 in Ref. [24]).

To study the correlated electronic behavior in the sample, we perform ODRC measurements at 3 K. A dc voltage applied to the top gate (V_{tg}) is used to tune the carrier concentration in region I, and an ac voltage ($\Delta\tilde{V}$) induces charge redistribution between regions I and II. A probe laser in resonance with the lowest-energy WSe_2 exciton peak is used to measure charge flow in the sample [18] (see Fig. S4 of Supplemental Material for details [24]). Figure 1(d) shows the measured ODRC signals as a function of V_{tg} at two excitation frequencies. Consistent with the previous

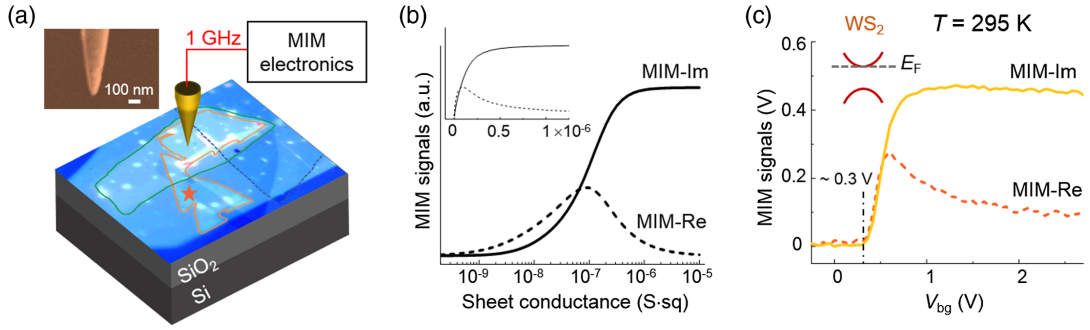

FIG. 2. (a) Schematic diagram of the TF MIM measurements on the WSe_2/WS_2 heterobilayer device. The inset shows the SEM image of the etched tungsten tip. (b) FEA simulated MIM signals as a function of the sheet conductance of the buried TMD layers. The inset shows the same plot in the linear scale. (c) Measured room-temperature MIM signals on the WS_2 monolayer [orange star in (a)] as a function of the back-gate voltage. The black dash-dotted line indicates the charge-neutral point for electrons at ~0.3 V, where the Fermi level resides at the conduction band minimum (inset).

report [17,18], a prominent dip in the change of optical contrast is observed at $V_{tg} \sim -1.37$ V, corresponding to a filling factor $n/n_0 = -1$ or one hole per moiré unit cell (n represents the charge concentration and $n_0 = 1/[L_M^2 \sin(\pi/3)] \sim 1.8 \times 10^{12}$ cm^{-2} is the density of one charge per moiré unit cell). In addition to this Mott state, a satellite dip also appears at factional filling $n/n_0 = -1/3$.

The nanoscale conductivity of the moiré superlattice device is studied by microwave impedance microscopy (MIM) [32], a versatile technique for imaging the spatial uniformity of electrical properties in advanced materials [33–36]. As shown in Fig. 2(a), a microwave signal (~10 μW at 1 GHz) is delivered to a chemically etched tungsten tip, which is mounted on a quartz tuning fork (TF) for distance feedback [37–38]. The two MIM output signals, proportional to the imaginary (MIM-Im) and real (MIM-Re) parts of the tip-sample admittance, are demodulated at the TF resonant frequency (~37 kHz). The spatial resolution is on the order of 100 nm, which is comparable to the tip diameter, as shown in the scanning electron microscopy (SEM) image in Fig. 2(a). The MIM response to the sheet conductance of a buried 2D layer can be modeled by finite element analysis (FEA) [32]. Figure 2(b) shows the simulated MIM result as a function of the 2D conductance σ of, e.g., the WS_2 monolayer in both semilog (main plot) and linear (inset) scales. Note that the MIM-Im signal increases monotonically with increasing σ, whereas MIM-Re peaks at $\sigma \sim 10^{-7}$ S sq (see Fig. S5 for details in Supplemental Material [24]). For comparison, the measured room-temperature MIM signals as a function of the back-gate voltage (V_{bg}) in the monolayer WS_2 region are shown in Fig. 2(c). Below a threshold voltage of ~0.3 V, MIM signals in both channels are negligible, indicating the absence of mobile carriers when the Fermi level is inside the semiconducting gap. For $V_{bg} > 0.3$ V, the electrostatic doping occurs, as evidenced by the increase of MIM signals. The close resemblance between the simulated [Fig. 2(b) inset] and measured [Fig. 2(c)] results suggests that the device behaves as a regular back-gated field-effect transistor (FET). For simplicity, we will in the following only present the MIM-Im data because of its monotonic relationship with respect to the local conductance. A complete set of the MIM data are found in Fig. S6 in Supplemental Material [24].

The cryogenic MIM experiment is carried out in a helium-flow cryostat with a base temperature ~20 K. Figure 3(a) displays the sample topography taken by the TF feedback, where some surface impurities or air bubbles are clearly visible. The simultaneously acquired MIM-Im image at $V_{bg} = 0$ V and $T = 24$ K [Fig. 3(b)] shows that only the contact and top-gate FLG regions are conductive. Strikingly, while the individual TMD layers and the heterostructure (HS) region are both highly insulating at zero V_{bg}, they exhibit very different gate dependences. As seen in the inset of Fig. 3(b), monolayer WSe_2 is conductive at $V_{bg} = -2$ V due to the electrostatic doping of holes. The HS region, however, is strongly insulating. Such an unusual behavior of the WSe_2/WS_2 bilayer is beyond the simple description of a back-gated FET and worth further investigation.

Since the vertically stacked layers are relatively fragile and could be easily damaged by repeated scans, we focus on point measurements for systematic studies of the gate dependence. Figure 3(c) shows the MIM-Im response on three points (WS_2, WSe_2, and HS) indicated in Fig. 3(a) when V_{bg} is swept from −2.7 to 2.7 V. The ambipolarlike FET behavior is observed in both monolayers. We notice that the WS_2 layer is much more difficult to turn on with hole doping, similar to previous FET studies [39–42]. In the HS region, on the other hand, two prominent drops of MIM-Im signals appear at around $V_{bg} \sim -2.1$ V and +1.8 V. On the hole-doped side, given the threshold voltage $V_{th} \sim -0.7$ V for injecting holes into the WSe_2 layer, the insulating state corresponds to a filling factor $n/n_0 = -1$, i.e., one hole per moiré unit cell. The results are also consistent with the ODRC data [Fig. 1(d)] and previous investigations [17,18].

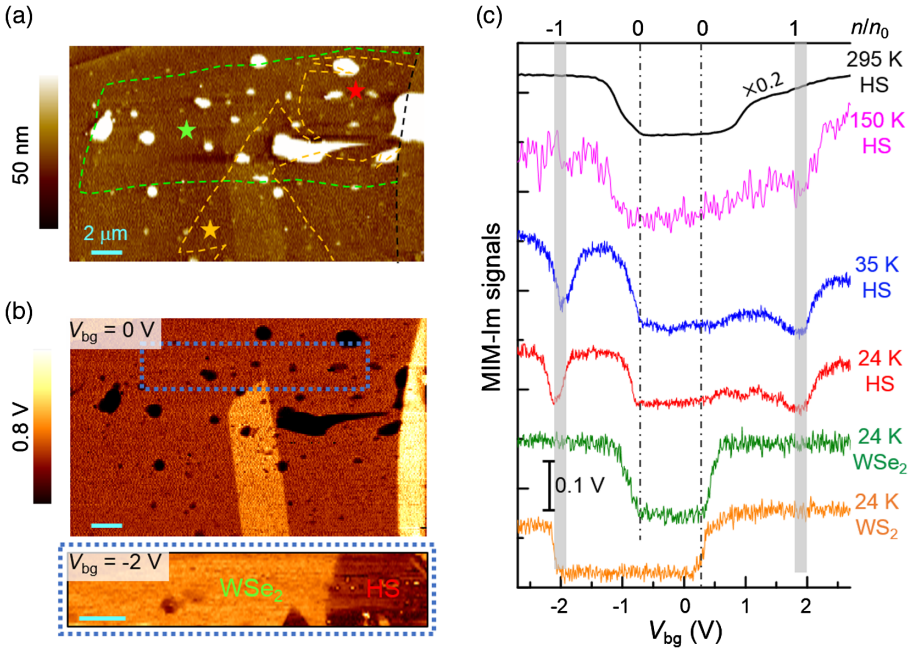

FIG. 3. (a) Topographic image of the WSe_2/WS_2 device taken by the tuning-fork feedback. The WSe_2, WS_2, and top FLG regions are labeled by green, orange, and black dashed lines, respectively. The green, orange, and red stars mark the locations where the MIM curves in (c) are taken. (b) MIM-Im image at $T = 24$ K and $V_{bg} = 0$ V in the same area as (a). Inset: MIM-Im images in the blue dashed box in (b) taken at $V_{bg} = -2$ V. Scale bars in (a) and (b) are 2 μm. (c) MIM-Im signals at various locations and temperature. The two dash-dotted lines denote the charge-neutral points, -0.7 V for holes in WSe_2 and $+0.3$ V for electrons in WS_2. The shaded areas correspond to the Mott insulating states at $n/n_0 = \pm 1$. The data at 295K HS is scaled by 0.2 for compact visualization.

The difference in the voltage values is because the ODRC measurements use the top gate with the top HBN thickness of 11 nm and the MIM measurements use the bottom gate with the bottom HBN thickness of 16 nm. Note that the MIM imaging was performed at a higher temperature (24 K) than the ODRC measurement (3 K). Therefore, the absence of the weak $-1/3$ state [Fig. 1(d)], which develops at lower temperatures than the Mott insulating states [17,18,43], in the MIM data is most likely due to the thermal activation effect.

The insulating state with electron doping, however, has not been observed before. Since both WSe_2 and WS_2 are turned on at $V_{th} = 0.2$–0.3 V, it is reasonable to assume that gate-induced electrons are injected to the heterostructure region at the same threshold voltage. Similar to the hole-doped side, the observed insulating state at $V_{bg} \sim 1.8$ V corresponds to filling factor $n/n_0 = +1$, i.e., one electron per moiré unit cell. Interestingly, while the two monolayer regions display comparable MIM-Im signals in the ambipolar FET curves, the overall MIM signal level on the electron-doped side is considerably lower than that on the hole-doped side, indicative of a large intrinsic resistance of the former. Such a property may lead to large contact resistance, which represents a big challenge for conventional transport measurements to access the electron side of WSe_2/WS_2 moiré superlattices at low doping and low temperatures. On the other hand, it is also possible that such asymmetry between electron and hole doping is specific to near-60° WSe_2/WS_2 samples, as the phenomenon is not observed in a recent MIM report [44] on a near-0° device. Further experiments on twist-angle-dependent TMD moiré devices are needed to examine this hypothesis. We emphasize that the requirement of good Ohmic contacts is much less stringent for the MIM measurements, which enables the observation of Mott states on both electron and hole sides. The Mott states persist up to ~150 K and eventually vanish at 295 K. A rough estimate of the thermal activation gap of the Mott state is thus 10–20 meV, consistent with the earlier reports [17,18]. Similar results are observed on another WSe_2/WS_2 heterostructure device with near-0° twist angle (see Fig. S7 in Supplemental Material [24]), consistent with the previous investigations [17,21] that correlated electron physics occurs in both 0° and 60° twist-angle moiré superlattices. Note that the slightly different stacking configurations in these two types of samples (see Fig. S8 in Ref. [24]) might lead to a moderate difference in local band reconstructions [45], awaiting systematic theoretical and experimental investigations on this topic.

Finally, we briefly discuss the spatial variation of the Mott insulating state in the moiré superlattice. Figures 4(a) and 4(b) show the close-up AFM and MIM-Im images near the HS region at $T = 24$ K and $V_{bg} = -2$ V. In addition to the surface impurities visible from the topography, inhomogeneous local conductivity is clearly observed in the MIM image. In Fig. 4(c), the MIM-Im signals when V_{bg} is swept from -2.7 to 2.7 V are plotted for the three points

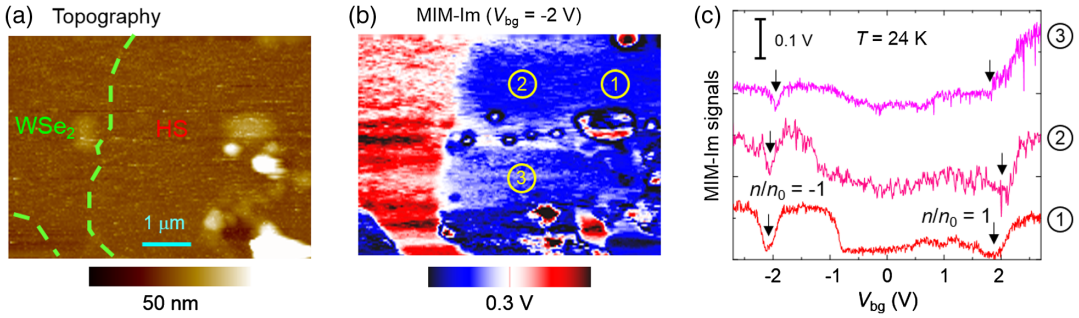

FIG. 4. (a) Topography and (b) MIM-Im images at $V_{bg} = -2$ V for a close-up view in the heterostructure region. (c) MIM-Im signals at three different locations labeled in (b) as a function of the back-gate voltage. The positions of $n/n_0 = \pm 1$ are indicated by arrows for each curve. For line No. 3 where the $n/n_0 = 1$ state is not fully developed, the arrow denotes the location where the slope changes sign.

labeled in Fig. 4(b). The dips for $n/n_0 = \pm 1$, although present in all curves, differ significantly in their strengths and positions with respect to V_{bg}. The electrical inhomogeneity is indicative of spatial disorder in the correlated insulating state, which may be caused by strains, defects, and density inhomogeneity from electrostatic gating. In Fig. 4(c), the variation of $\Delta V_{bg} \sim 0.2$ V where Mott states are observed is mostly associated with local fluctuations of the carrier density $\Delta n \sim 0.24 \times 10^{12}$ cm^{-2}. The large variations in the strength and linewidth of the MIM dips of $n/n_0 = \pm 1$ also indicate the presence of strong fluctuation in moiré potentials. Further theoretical and experimental efforts are needed to quantify such effects. We emphasize that, unlike the situation in graphene moiré systems, correlated states in WSe_2/WS_2 with large lattice mismatch and small superlattice constant is less sensitive to twist-angle disorders. The small angular misalignment would not induce significant changes on the moiré periodicity and local properties in this study. In fact, away from large surface impurities and air bubbles, the moiré periodicity is highly uniform in the mesoscopic length scale of 50–100 nm probed by the MIM, as indicated by our scanning tunneling microscopy data [46]. Future improvement on the sample uniformity, such as reducing surface impurities in the 2D stack and better gating schemes, is thus critical for in-depth understanding of correlation physics in 2D moiré superlattices.

In summary, we report the near-field microwave imaging of correlated states in semiconducting TMD heterobilayer moiré superlattices. The ability to probe local conductivity in buried structures allows us to observe the Mott insulating phases with both hole and electron doping at temperatures up to 150 K. The nanoscale microwave images reveal substantial spatial inhomogeneity in the correlated states. Our work provides a guideline for improving the material quality toward novel electronic states in 2D moiré systems.

The work at UT-Austin (Z. C., X. M., and Z. X., and K. L.) was supported by the U.S. Department of Energy (DOE), Office of Science, Basic Energy Sciences, under Award No. DE-SC0019025. The MIM instrumentation is supported by the Welch Foundation Grant No. F-1814. The ODRC measurements are supported by the Director, Office of Science, Office of Basic Energy Sciences, Materials Sciences and Engineering Division of the U.S. Department of Energy under Contract No. DE-AC02-05CH11231 (van der Waals heterostructures program, KCWF16). The heterostructure fabrication is supported by the U.S. Army Research Office under MURI Grant No. W911NF-17-1-0312. K. W. and T. T. acknowledge support from the Elemental Strategy Initiative conducted by the MEXT, Japan, Grant No. JPMXP0112101001, JSPS KAKENHI Grant No. JP20H00354 and the CREST (JPMJCR15F3), JST. S. T acknowledges support from DOE-SC0020653, NSF DMR 1552220, DMR 1904716, and NSF CMMI 1933214. E. C. R. acknowledges support from the Department of Defense (DoD) through the National Defense Science & Engineering Graduate Fellowship (NDSEG) Program. The authors also thank H. Li and S. Li for sharing unpublished scanning tunneling microscopy results on WSe_2/WS_2 samples.

*These authors contributed equally to this work.
†Corresponding author.
fengwang76@berkeley.edu
‡Corresponding author.
kejilai@physics.utexas.edu

[1] J. M. B. L. dos Santos, N. M. R. Peres, and A. H. C. Neto, Phys. Rev. Lett. **99**, 256802 (2007).
[2] R. Bistritzer and A. H. MacDonald, Proc. Natl. Acad. Sci. U.S.A. **108**, 12233 (2011).
[3] M. Yankowitz, J. Xue, D. Cormode, J. D. Sanchez-Yamagishi, K. Watanabe, T. Taniguchi, P. Jarillo-Herrero, P. Jacquod, and B. J. LeRoy, Nat. Phys. **8**, 382 (2012).
[4] Y. Cao, V. Fatemi, A. Demir, S. Fang, S. L. Tomarken, J. Y. Luo, J. D. Sanchez-Yamagishi, K. Watanabe, T. Taniguchi, E. Kaxiras, R. C. Ashoori, and P. Jarillo-Herrero, Nature (London) **556**, 80 (2018).
[5] Y. Cao, V. Fatemi, S. Fang, K. Watanabe, T. Taniguchi, E. Kaxiras, and P. Jarillo-Herrero, Nature (London) **556**, 43 (2018).

[6] G. Chen, L. Jiang, S. Wu, B. Lyu, H. Li, B. L. Chittari, K. Watanabe, T. Taniguchi, Z. Shi, J. Jung, Y. Zhang, and F. Wang, Nat. Phys. **15**, 237 (2019).
[7] G. Chen, A. L. Sharpe, P. Gallagher, I. T. Rosen, E. J. Fox, L. Jiang, B. Lyu, H. Li, K. Watanabe, T. Taniguchi, J. Jung, Z. Shi, D. Goldhaber-Gordon, Y. Zhang, and F. Wang, Nature (London) **572**, 215 (2019).
[8] X. Lu, P. Stepanov, W. Yang, M. Xie, M. A. Aamir, I. Das, C. Urgell, K. Watanabe, T. Taniguchi, G. Zhang, A. Bachtold, A. H. MacDonald, and D. K. Efetov, Nature (London) **574**, 653 (2019).
[9] M. Yankowitz, S. Chen, H. Polshyn, Y. Zhang, K. Watanabe, T. Taniguchi, D. Graf, A. F. Young, and C. R. Dean, Science **363**, 1059 (2019).
[10] A. L. Sharpe, E. J. Fox, A. W. Barnard, J. Finney, K. Watanabe, T. Taniguchi, M. A. Kastner, and D. Goldhaber-Gordon, Science **365**, 605 (2019).
[11] G. Chen, A. L. Sharpe, E. J. Fox, Y. H. Zhang, S. Wang, L. Jiang, B. Lyu, H. Li, K. Watanabe, T. Taniguchi, Z. Shi, T. Senthil, D. Goldhaber-Gordon, Y. Zhang, and F. Wang, Nature (London) **579**, 56 (2020).
[12] M. Serlin, C. L. Tschirhart, H. Polshyn, Y. Zhang, J. Zhu, K. Watanabe, T. Taniguchi, L. Balents, and A. F. Young, Science **367**, 900 (2020).
[13] F. Wu, T. Lovorn, E. Tutuc, and A. H. MacDonald, Phys. Rev. Lett. **121**, 026402 (2018).
[14] J. Hubbard, Proc. R. Soc. A **276**, 238 (1963).
[15] A. Singha, M. Gibertini, B. Karmakar, S. Yuan, M. Polini, G. Vignale, M. I. Katsnelson, A. Pinczuk, L. N. Pfeiffer, K. W. West, and V. Pellegrini, Science **332**, 1176 (2011).
[16] L. Wang, E. Shih, A. Ghiotto, L. Xian, D. A. Rhodes, C. Tan, M. Claassen, D. M. Kennes, Y. Bai, B. Kim, K. Watanabe, T. Taniguchi, X. Zhu, J. Hone, A. Rubio, A. Pasupathy, and C. R. Dean, Nat. Mater. **19**, 861 (2020).
[17] Y. Tang, L. Li, T. Li, Y. Xu, S. Liu, K. Barmak, K. Watanabe, T. Taniguchi, A. H. MacDonald, J. Shan, and K. F. Mak, Nature (London) **579**, 353 (2020).
[18] E. C. Regan, D. Wang, C. Jin, M. I. B. Utama, B. Gao, X. Wei, S. Zhao, W. Zhao, Z. Zhang, K. Yumigeta, M. Blei, J. D. Carlström, K. Watanabe, T. Taniguchi, S. Tongay, M. Crommie, A. Zettl, and F. Wang, Nature (London) **579**, 359 (2020).
[19] H. Pan, F. Wu, and S. D. Sarma, arXiv:2004.04168.
[20] A. Uri1, S. Grover, Y. Cao, J. A. Crosse, K. Bagani, D. Rodan-Legrain, Y. Myasoedov, K. Watanabe, T. Taniguchi, P. Moon, M. Koshino, P. Jarillo-Herrero, and E. Zeldov, Nature (London) **581**, 47 (2020).
[21] M. H. Naik and M. Jain, Phys. Rev. Lett. **121**, 266401 (2018).
[22] E. S. Kadantsev and P. Hawrylak, Solid State Commun. **152**, 909 (2012).
[23] B. Fallahazad, H. C. P. Movva, K. Kim, S. Larentis, T. Taniguchi, K. Watanabe, S. K. Banerjee, and E. Tutuc, Phys. Rev. Lett. **116**, 086601 (2016).
[24] See Supplemental Material at http://link.aps.org/supplemental/10.1103/PhysRevLett.125.186803 for device fabrication, more experimental data, and details of analysis, which includes Refs. [25–30].
[25] L. Wang, I. Meric, P. Y. Huang, Q. Gao, Y. Gao, H. Tran, T. Taniguchi, K. Watanabe, L. M. Campos, D. A. Muller, J. Guo, P. Kim, J. Hone, K. L. Shepard, and C. R. Dean, Science **342**, 614 (2013).
[26] N. Kumar, S. Najmaei, Q. Cui, F. Ceballos, P. M. Ajayan, J. Lou, and H. Zhao, Phys. Rev. B **87**, 161403(R) (2013).
[27] Y. Li, Y. Rao, K. F. Mak, Y. You, S. Wang, C. R. Dean, and T. F. Heinz, Nano Lett. **13**, 3329 (2013).
[28] A. Laturia, M. L. Van de Put, and W. G. Vandenberghe, NPJ 2D Mater. Appl. **2**, 6 (2018).
[29] S. Bellucci, A. Maffucci, S. Maksimenko, F. Micciulla, M. D. Migliore, A. Paddubskaya, D. Pinchera, and F. Schettino, Materials **11**, 2519 (2018).
[30] K. Murase, Jpn. J. Appl. Phys **33**, 1385 (1994).
[31] C. Jin, E. C. Regan, A. Yan, M. I. B. Utama, D. Wang, S. Zhao, Y. Qin, S. Yang, Z. Zheng, S. Shi, K. Watanabe, T. Taniguchi, S. Tongay, A. Zettl, and F. Wang, Nature (London) **567**, 76 (2019).
[32] K. Lai, W. Kundhikanjana, M. Kelly, and Z. X. Shen, Rev. Sci. Instrum. **79**, 063703 (2008).
[33] K. Lai, H. Peng, W. Kundhikanjana, D. T. Schoen, C. Xie, S. Meister, Y. Cui, M. A. Kelly, and Z. X. Shen, Nano Lett. **9**, 1265 (2009).
[34] D. Wu, X. Li, L. Luan, X. Wu, W. Li, M. N. Yogeesh, R. Ghosh, Z. Chu, D. Akinwande, Q. Niu, and K. Lai, Proc. Natl. Acad. Sci. U.S.A. **113**, 8583 (2016).
[35] Z. Chu, L. Zheng, and K. Lai, Annu. Rev. Mater. Res. **50**, 105 (2020).
[36] Z. Chu, C. Wang, J. Quan, C. Zhang, C. Lei, A. Han, X. Ma, H. Tang, D. Abeysinghe, M. Staab, X. Zhang, A. H. MacDonald, V. Tung, X. Li, C. Shih, and K. Lai, Proc. Natl. Acad. Sci. U.S.A. **117**, 13908 (2020).
[37] Y. Cui, E. Y. Ma, and Z. X. Shen, Rev. Sci. Instrum. **87**, 063711 (2016).
[38] X. Wu, Z. Hao, D. Wu, L. Zheng, Z. Jiang, V. Ganesan, Y. Wang, and K. Lai, Rev. Sci. Instrum. **89**, 043704 (2018).
[39] D. Braga, I. G. Lezama, H. Berger, and A. F. Morpurgo, Nano Lett. **12**, 5218 (2012).
[40] B. W. H. Baugher, H. O. H. Churchill, Y. Yang, and P. Jarillo-Herrero, Nat. Nanotechnol. **9**, 262 (2014).
[41] Y. J. Zhang, T. Oka1, R. Suzuki, J. T. Ye, and Y. Iwasa, Science **344**, 725 (2014).
[42] D. Ovchinnikov, A. Allain, Y. Huang, D. Dumcenco, and A. Kis, ACS Nano **8**, 8174 (2014).
[43] Y. Xu, S. Liu, D. A. Rhodes, K. Watanabe, T. Taniguchi, J. Hone, V. Elser, K. F. Mak, and J. Shan, arXiv:2007.11128.
[44] X. Huang, T. Wang, S. Miao, C. Wang, Z. Li, Z. Lian, T. Taniguchi, K. Watanabe, S. Okamoto, D. Xiao, S. Shi, and Y. Cui, arXiv:2007.11155.
[45] Z. Zhang, Y. Wang, K. Watanabe, T. Taniguchi, K. Ueno, E. Tutuc, and B. J. LeRoy, Nat. Phys. (2020) https://doi.org/10.1038/s41567-020-0958-x.
[46] H. Li, S. Li, and F. Wang (private communications).